Chemical Engineering Journal 490 (2024) 151932

Contents lists available at ScienceDirect

Chemical Engineering Journal

journal homepage: www.elsevier.com/locate/cej

Activation of peracetic acid by a magnetic biochar-ferrospinel AFe_2O_4 (A = Cu, Co, or Mn) nanocomposite for the degradation of carbamazepine – A comparative and mechanistic study

Yongtao Xue [a], Mohammadreza Kamali [a], Babak Kakavandi [b], Maria Elisabete V. Costa [c], Ian P. Thompson [d], Wei Huang [d], Lise Appels [a], Raf Dewil [a,d,*]

[a] KU Leuven, Department of Chemical Engineering, Process and Environmental Technology Lab, J. De Nayerlaan 5, 2860 Sint-Katelijne-Waver, Belgium
[b] Alborz University of Medical Sciences, Department of Environmental Health Engineering, Karaj, Iran
[c] University of Aveiro, Department of Materials and Ceramics Engineering, Aveiro Institute of Materials, CICECO, 3810-193 Aveiro, Portugal
[d] University of Oxford, Department of Engineering Science, Parks Road, Oxford OX1 3PJ, United Kingdom

ARTICLE INFO

Keywords:
Peracetic acid
Biochar
Spinel ferrite
Carbamazepine
Comparative study
Mechanisms

ABSTRACT

Peracetic acid (PAA)-based advanced oxidation processes (AOPs) are promising technologies for the efficient treatment of persistent contaminants in wastewater. In this study, three different magnetic biochar (BC)-ferrospinel AFe_2O_4 (A = Cu, Co, or Mn) nanocomposites were synthesized through a combined sol–gel/pyrolysis process for the activation of PAA to degrade carbamazepine (CBZ). The following order of efficiency was observed for CBZ degradation in the presence of PAA: BC-$CoFe_2O_4$ (100 %) > BC-$MnFe_2O_4$ (7 %) ≈ BC-$CuFe_2O_4$ (7 %). In addition, 0.8 mM PAA, 0.3 g/L catalyst, nearly neutral pH, and 333 K were identified as the optimal operating parameters for the degradation of 1 mg/L CBZ in the BC-$CoFe_2O_4$/PAA system. Mechanistic studies revealed that $CH_3C(O)OO^{\bullet}$ radicals are the dominant active species for the degradation of CBZ in the BC-$CoFe_2O_4$/PAA system, and the continuous conversion of Co(II) to Co(III) in this system is responsible for the generation of these radicals. In addition, the water matrices (e.g., humic acid (20 mg/L), NaCl (0.05 M), and $NaNO_3$ (0.01 M)) played negligible roles in the degradation of CBZ in the BC-$CoFe_2O_4$/PAA system. This system exhibited highly selective and reactive degradation of organic pollutants with electron-rich groups (e.g., CBZ (0.36 min^{-1}), sulfamethoxazole (0.12 min^{-1}), and diclofenac (0.28 min^{-1})). Furthermore, the degradation products of CBZ were identified, and possible degradation pathways and toxicity of these transformation products were proposed. The BC-$CoFe_2O_4$/PAA system demonstrated outstanding degradation performance in dynamic systems and real wastewater treatment applications. This study describes the performance of an efficient and easy-to-separate catalyst for the activation of PAA. This study facilitates the development and application of PAA-based AOPs for wastewater treatment.

1. Introduction

Carbamazepine (CBZ) is a typical pharmaceutically active compound (PhAC) that is frequently detected in a variety of water systems due to its non-biodegradable and persistent molecular structure. In addition, long-term exposure to CBZ can have adverse effects on aquatic organisms and humans, such as endocrine disruption and teratogenicity [1]. Recently, advanced oxidation processes (AOPs) have been comprehensively studied for the elimination of emerging contaminants in wastewater treatment applications [2]. In particular, peracetic acid (PAA, $CH_3C(O)OOH$) has been widely used as a disinfectant in various applications (e.g., the food industry, health care, and paper industry) due to its high redox potential (1.06–1.96 V), excellent sterilization ability, and low toxicity for disinfecting byproducts [3,4]. PAA-based AOPs have been suggested for the treatment of recalcitrant organic pollutants such as pharmaceutically active compounds (PhACs, e.g., sulfamethoxazole (SMX) [5], carbamazepine (CBZ) [6], and diclofenac (DCF) [7]). From a mechanistic point of view, the homolysis of the peroxyl bond (O–O) in PAA generates $^{\bullet}OH$ and various R–$O^{\bullet}$ (e.g., $CH_3C(O)OO^{\bullet}$, $CH_3C(O)O^{\bullet}$, $CH_3O_2^{\bullet}$, $^{\bullet}CH_3$) radicals, which are responsible for the degradation of

* Corresponding author at: KU Leuven, Department of Chemical Engineering, Process and Environmental Technology Lab, J. De Nayerlaan 5, 2860 Sint-Katelijne-Waver, Belgium.
E-mail address: raf.dewil@kuleuven.be (R. Dewil).

https://doi.org/10.1016/j.cej.2024.151932
Received 25 January 2024; Received in revised form 27 April 2024; Accepted 4 May 2024
Available online 4 May 2024

organic pollutants in such systems [8]. PAA exhibits a much lower O–O bond energy (159 kJ/mol) than commonly used H_2O_2 (213 kJ/mol) and peroxymonosulfate (PMS, 317 kJ/mol), indicating that the activation process of PAA is thermodynamically more straightforward [9].

Recently, various methods have been developed to activate PAA to degrade organic pollutants in wastewater treatment applications. Additionally, the dominant active species generated in PAA-based degradation processes are highly dependent on the activation approach used [10]. For instance, Yan et al. [11] reported that $^{\bullet}OH$ is the crucial radical for the degradation of oxytetracycline in the UV/PAA system. Yao et al. [12] reported that singlet oxygen and R–$O^{\bullet}$ were the dominant active species for the degradation of tetracycline hydrochloride in an ultrasound/PAA system. In transition metal-based PAA systems, electron transfer between the metal and PAA is the primary mechanism involved in the generation of such active species (M^{n+} + $CH_3C(O)OOH \rightarrow M^{(n+1)+}$ $CH_3C(O)O^{\bullet}$ + OH^-, $M^{(n+1)+}$ + $CH_3C(O)OOH \rightarrow M^{n+}$ + $CH_3C(O)OO^{\bullet}$ + H^+) [13]. Among all PAA activation processes, the use of transition metals is considered a promising way to address recalcitrant organic compounds because of their powerful oxidation abilities and high selectivity of R–$O^{\bullet}$ radicals toward organic contaminants, as well as their facile and cost-effective process [14]. Spinel ferrite is defined as a metal oxide comprising a spine structure with a general molecular formula of AFe_2O_4 (A is a positive divalent ion, such as Cu^{2+}, Co^{2+}, Mn^{2+}, Ni^{2+}, Zn^{2+}). The application of these materials is currently under the spotlight due to their high efficiency and cost-effectiveness. For instance, Yu et al. [15] successfully synthesized $CuFe_2O_4$ for the activation of PAA, and this system demonstrated excellent degradation efficiency (100 %) for the decomposition of rhodamine B. Additionally, Wang et al. [16] reported that the $CoFe_2O_4$/PAA system exhibits a high degradation efficiency (87 %) for sulfamethoxazole under near-neutral conditions.

Although spinel ferrite materials can be easily separated from water due to their magnetic properties, the leaching of heavy metal ions from nanomaterials into water is still a challenging issue, demanding further studies. The agglomeration of magnetic nanomaterials also restricts their degradation efficiency by reducing the number of available active sites on the surface of catalytic materials [17]. Some approaches have been investigated to address these issues, such as the immobilization of catalytic materials into a support structure. Biochar (BC) is a low-cost and environmentally friendly material derived from waste resources (e.g., biomass) with tunable properties, such as the concentration of surface functional groups and high specific surface area and porosity [18]. Hence, BC-supported spinel ferrite nanomaterials are expected to efficiently activate PAA and reduce the leaching of metal ions from catalytic materials. Dong et al. [19] demonstrated that lignin-derived biochar-$CoFe_2O_4$ has high stability and can efficiently activate PAA for the degradation of sulfamethoxazole. In addition, the various spinel ferrite materials have different efficiencies for the degradation of organic pollutants. For instance, Gupta et al. [20] reported an advanced reduction process (ARP) for the elimination of nitrophenols using various spinel ferrite materials, demonstrating the following order of efficiency: $CuFe_2O_4$ > $MnFe_2O_4$ > $CoFe_2O_4$ > $NiFe_2O_4$. Ren et al. [21] observed that the degradation efficiency of di-n-butyl phthalate in a spinel ferrite material/peroxymonosulfate (PMS) system, a well-known AOP process, follows the order of $CoFe_2O_4$ > $CuFe_2O_4$ > $MnFe_2O_4$ > $ZnFe_2O_4$. However, to the best of our knowledge, there are no available studies that compare different BC-supported spinel ferrite materials for the activation of PAA to degrade organic pollutants in wastewater treatment applications.

In this study, magnetic biochar-ferrospinel AFe_2O_4 (A = Cu, Co, or Mn) nanocomposites were synthesized through a combined sol–gel/pyrolysis process. Their efficiencies were evaluated and compared for the degradation of carbamazepine (CBZ) as a target pollutant in the presence of PAA. The operating conditions were optimized to achieve the best degradation performance. In addition, CBZ degradation mechanisms were identified based on scavenging experiments, *in situ* ATR-FTIR, and electrochemical analysis. The effects of water matrices, including humic acid, NaCl, $NaHCO_3$, and $NaNO_3$, on the degradation of CBZ in the $CoFe_2O_4$/PAA system were also studied and discussed. Furthermore, the CBZ degradation pathways and the toxicity of the degradation products were proposed based on the results obtained from liquid chromatography–mass spectrometry, and the applicability for the degradation of various organic pollutants and the stability of the BC-$CoFe_2O_4$/PAA system were evaluated. Finally, tests were carried out in a continuous recirculation system to support further upscaling of the BC-$CoFe_2O_4$/PAA system.

2. Materials and methods

2.1. Chemicals

The details of the chemicals used in this study are provided in Text S1 in the Supporting information. All solutions were made in Milli-Q water.

2.2. Synthesis and characterization of materials

Magnetic biochar (BC)-ferrospinel AFe_2O_4 (A = Cu, Co, or Mn) nanocomposites were synthesized by a modified sol–gel method. All details are provided in Text S2. The composition and crystal structure of the materials, as well as their morphologies, surface area and porosity, available surface functional groups, electrochemical properties, and surface charge, were characterized by various characterization techniques according to the details provided in Text S3.

2.3. Experimental procedure

The details of the degradation experiments are provided in Text S4, and those of the analytical methods are provided in Text S5 in the Supporting information. The calculation methods for the degradation rate constant and activation energy are also provided in Text S6 in the Supporting information. The degradation products of CBZ were identified using ultrahigh-performance liquid chromatography coupled to a quadrupole time-of-flight mass spectrometer (UHPLC-QTOF) system, and the toxicity of these organic pollutants was predicted through the Toxicity Estimation Software Tool (T.E.S.T., EPA, US). More information about these can be found in Text S7 in the Supporting information.

3. Results and discussion

3.1. Characterization of the catalysts

Fig. 1a–c shows the XRD patterns of BC-$CuFe_2O_4$, BC-$CoFe_2O_4$, and BC-$MnFe_2O_4$, respectively. In Fig. 1a, the characteristic peaks located at 2θ values of 18.3°, 30.3°, 35.7°, 43.6°, 57.7°, and 62.3° are indexed to the (1 0 1), (2 0 0), (2 1 1), (2 2 0), (3 2 1), and (2 2 4) crystal planes of tetragonal $CuFe_2O_4$ (JCPDS card no. 34-0425), respectively [22]. In addition, the diffraction peaks appearing at 2θ values of 24.1°, 33.1°, 40.8°, 49.4°, and 54.1° are ascribed to the (0 1 2), (1 0 4), (1 1 3), (0 2 4), and (1 1 6) crystal planes of rhombohedral Fe_2O_3 (JCPDS card no. 24-0072), respectively [23]. Another peak at a 2θ value of 38.7° is related to the (1 1 1) crystal plane of the tenorite phase with a monoclinic CuO structure (JCPDS card no. 41-0254) [24]. Moreover, the peak intensity of $CuFe_2O_4$ is much greater than that of Fe_2O_3 and CuO, revealing that the contents of Fe_2O_3 and CuO in BC-$CuFe_2O_4$ are far lower than those in $CuFe_2O_4$. It has been reported that $CuFe_2O_4$ exists in two crystallographic forms, cubic and tetragonal structures; the cubic structure is stable below 300 °C, and the tetragonal structure is stable above 400 °C [25]. The appearance of the Fe_2O_3 and CuO phases can be attributed to the transformation of cubic $CuFe_2O_4$ to tetragonal $CuFe_2O_4$ ($2Fe^{3+}$ + 3CuO → Fe_2O_3 + $3Cu^{2+}$), which is a thermodynamically favorable process [26]. In Fig. 1b, the characterization peaks at 2θ values of 18.3°, 30.1°, 35.5°, 43.1°, 57.1°, and 62.6° are related to the

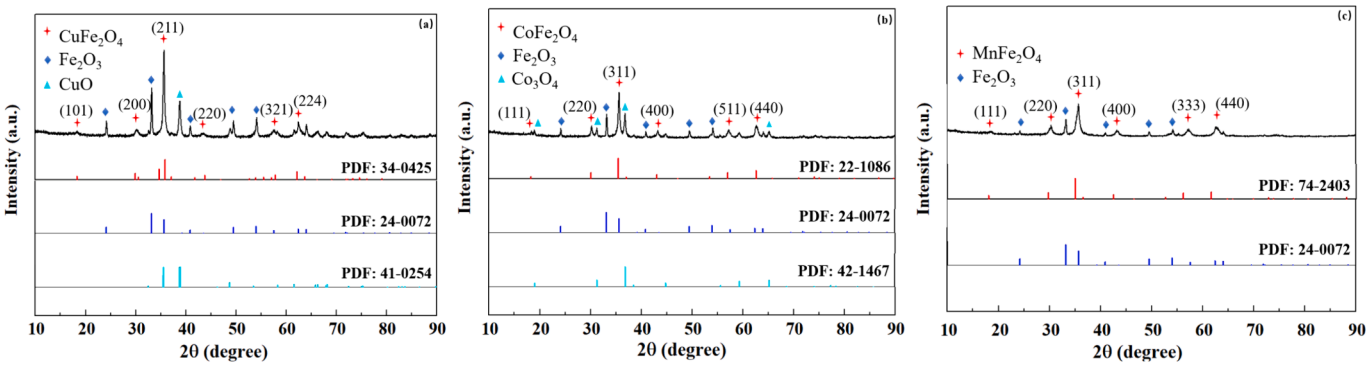

Fig. 1. XRD spectra of the prepared BC-$CuFe_2O_4$ (a), BC-$CoFe_2O_4$ (b), and BC-$MnFe_2O_4$ (c).

(111), (220), (311), (400), (511), and (440) crystal planes of cubic spinel of $CoFe_2O_4$ (JCPDS card no. 22-1086) [27], respectively, and the peaks at 2θ values of 18.9°, 31.1°, 36.8°, 65.1° are indexed to the (111), (220), (311), and (440) crystal planes of cubic spinel Co_3O_4 (JCPDS card no. 42-1467), respectively [28]. The $CoFe_2O_4$ peaks with higher intensities compared with those of Fe_2O_3 and Co_3O_4 suggest that $CoFe_2O_4$ is the main component of BC-$CoFe_2O_4$. In addition, the generation of Fe_2O_3 and Co_3O_4 may be due to the poorer homogeneity of the cation and walnut shell distribution, resulting in some cobalt-poor/abundant regions in the gel and leading to the formation of Fe_2O_3/Co_3O_4 [29]. Shi et al. [30] also reported that Fe_2O_3 existed in $CoFe_2O_4$ nanomaterials when the annealing temperature was lower than 700 °C through a traditional sol–gel synthesis process. In Fig. 1c, the diffraction peaks located at 18.4°, 30.3°, 35.6°, 43.1°, 57.3°, and 62.7° are ascribed to the (111), (220), (311), (400), (333), and (440) crystal planes of the cubic spinel of $MnFe_2O_4$ (JCPDS card no. 74-2403) [31], respectively. Additionally, slight Fe_2O_3 characterization peaks are observed in BC-$MnFe_2O_4$, which can be attributed to the decomposition of $MnFe_2O_4$ at high temperatures [32]. It has also been confirmed that relatively high temperatures favor the formation of Fe_2O_3 during the $MnFe_2O_4$ calcination process through a sol–gel method [33]. Moreover, the characterization peaks of BC cannot be observed among all the BC-$CuFe_2O_4$, BC-$CoFe_2O_4$, and BC-$MnFe_2O_4$ spectra because the high-intensity peaks of the catalytic materials (e.g., $CuFe_2O_4$ and CuO) mask the weak intensity peaks of BC.

The surface functional groups of the prepared nanomaterials were identified by interpreting the FTIR spectra. According to Fig. S1b–d, two peaks at approximately 1530 cm^{-1} and 1049 cm^{-1} appear in the spectra of all the BC, BC-$CuFe_2O_4$, BC-$CoFe_2O_4$, and BC-$MnFe_2O_4$ samples, which can be attributed to the vibrations of the N–H groups and C–O groups of BC [34,35], respectively. In addition, the peaks at approximately 535 cm^{-1} and 438 cm^{-1} are associated with the intrinsic stretching vibrations of metals at octahedral sites (Cu–O, Co–O or Mn–O) and the tetrahedral metal stretching of Fe–O [36], respectively. These results confirm the presence of these vibration bands in the BC-$CuFe_2O_4$, BC-$CoFe_2O_4$, and BC-$MnFe_2O_4$ composites. In addition, the N_2 adsorption–desorption isotherms and pore size distribution curves of BC-$CuFe_2O_4$, BC-$CoFe_2O_4$, and BC-$MnFe_2O_4$ are illustrated in Fig. S2. All isotherms of the prepared materials demonstrate a typical type IV isotherm with an H_3 hysteresis loop based on the IUPAC classification [37], confirming their mesoporous structures. In general, H_3-type hysteresis is generally observed on agglomerated particles forming plate slits, cracks, wedge-shaped structures, etc. [38]. Fig. S2b shows the broad pore size distribution of different types of nanomaterials in the composite nanomaterials. Furthermore, BC-$MnFe_2O_4$ represents the highest specific surface area and lowest average pore size (48 m^2/g, 10 nm) compared with BC-$CuFe_2O_4$ (22 m^2/g, 17 nm) and BC-$CoFe_2O_4$ (35 m^2/g, 14 nm) (Table S1). Furthermore, the morphologies and elemental

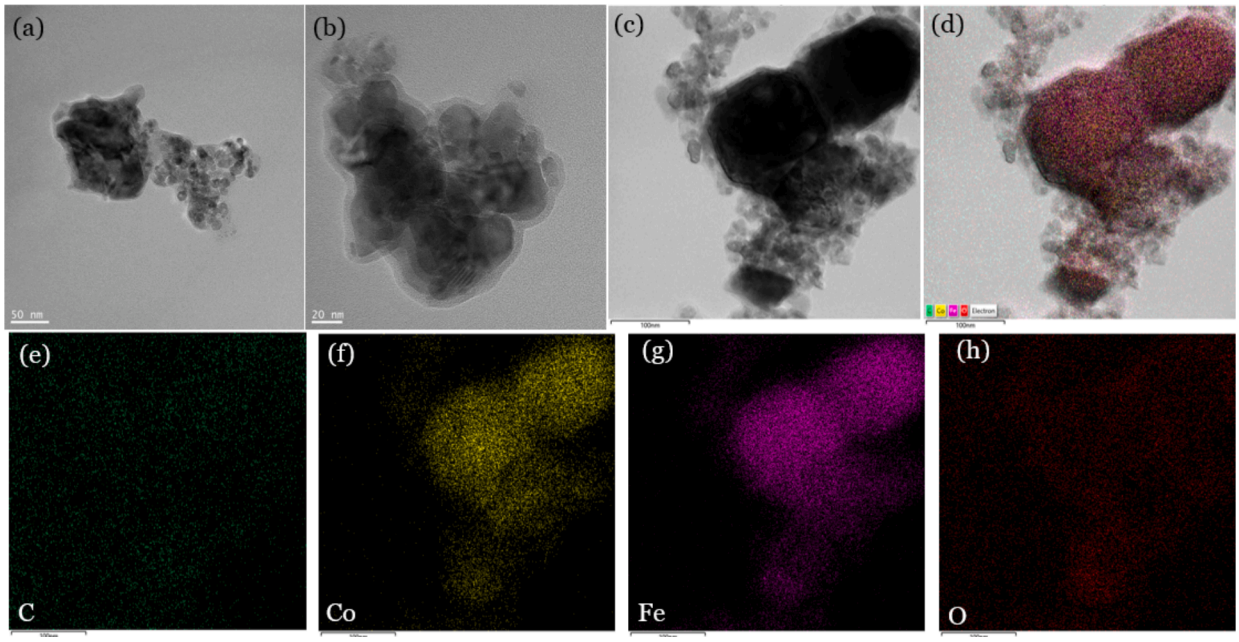

Fig. 2. TEM images of BC-$CoFe_2O_4$ (a–c) and elemental mapping of BC-$CoFe_2O_4$ (d–h).

compositions of the synthesized nanomaterials were investigated, as shown in Figs. 2 and S3. BC-$CoFe_2O_4$ had an irregular shape with 15 nm nanoparticles. The particle size distribution (PSD) test also showed that the particles formed agglomerates of approximately 460 nm (Table S2). The elemental mapping of the nanomaterials also confirmed that the materials contained C, Co, Fe, and O. Additionally, the TEM and mapping results of BC-$CuFe_2O_4$ and BC-$MnFe_2O_4$ also indicated nanosized particles and elemental compositions, respectively.

3.2. Removal of CBZ

The efficiency of the as-prepared nanocomposites in activating PAA to degrade CBZ was examined. Fig. 3a illustrates that all three synthesized nanocomposites demonstrate a negligible adsorption capacity for CBZ in 30 min, which can be related to their limited surface functional groups and porosity. They also represent different behaviors for the activation of PAA. BC-$CoFe_2O_4$ exhibited the highest CBZ degradation efficiency (100 %) in the presence of PAA, while both BC-$CuFe_2O_4$ (7 %) and BC-$MnFe_2O_4$ (7 %) were inactive in this process. Additionally, the degradation kinetics achieved with BC-$CoFe_2O_4$/PAA in this study are greater than those already reported in the literature for CBZ. Such a comparison is presented in Table S3. In addition, commercial PAA typically contains relatively low concentrations of H_2O_2. However, according to the background experiments performed (Fig. S4), no significant degradation efficiency for CBZ can be expected for the AFe_2O_4/H_2O_2 system, confirming that PAA plays a crucial role in the degradation of CBZ in the BC-$CoFe_2O_4$/PAA system. Further experiments were also conducted to study whether PAA can be self-activated for the degradation of CBZ. For this purpose, the concentrations of residual PAA with and without the catalysts were measured using UV–Vis spectroscopy, as described in the Supporting information. According to the results (Figs. S5 and S6), the self-decomposition of PAA was negligible, and the lowest residual concentration of this oxidation agent was detected in the BC-$CoFe_2O_4$ (46 % of the initial concentration) system, followed by BC-$MnFe_2O_4$ (68 %) and BC-$CuFe_2O_4$ (87 %). This reveals that more active species can be generated for the degradation of CBZ in the BC-$CoFe_2O_4$/PAA system. The higher efficiency of BC-$CoFe_2O_4$ compared to that of the other catalysts is mainly attributed to the presence of Co in its composition. To further confirm this hypothesis, homogenous catalytic activation of PAA with different metal ions, including Co, Mn, Cu, and Fe, was also performed to degrade CBZ. According to the results (Fig. S7a), Co^{2+} (1 mM) displayed an excellent degradation efficiency (100 %, 2 min) for CBZ compared with Cu^{2+} (5 %, 20 min) and Mn^{2+} (20 %, 20 min) in the presence of PAA, confirming that Co^{2+} is the most efficient catalyst among those studied in the present research. Furthermore, the addition of Fe^{3+} did not efficiently improve the degradation performance of the Cu^{2+} (or Co^{2+} or Mn^{2+})/Fe^{3+}/PAA systems (Fig. S7b). According to the literature [39], a high electron transfer rate in the catalyst also promotes nonradical pathways during the degradation of organic pollutants. This is due to the generation of more electrons, leading to the production of species such as singlet oxygen in the medium. In the present study, the cyclic voltammetry curves (Fig. S8) of the prepared nanomaterials demonstrated that BC-$MnFe_2O_4$ has the highest current density. In contrast, BC-$CuFe_2O_4$ has the lowest current density under the same conditions, indicating that BC-$MnFe_2O_4$ has excellent electron transfer performance. BC-$MnFe_2O_4$ also exhibited the highest specific surface area, highest electron transfer capacity, and 32 % decomposition ratio of PAA, while it only presented a 7 % degradation efficiency for CBZ. This is mainly because Mn^{2+} efficiently quenches peroxy radicals (e.g., $CH_3C(O)OO^{\bullet}$ and $CH_3C(O)O^{\bullet}$) through an electron transfer reaction with a reaction rate constant of $10^5 \sim 10^6$ M^{-1} S^{-1} [40], resulting in a low degradation efficiency of CBZ because fewer active species are involved in the CBZ degradation process.

3.3. Effects of critical factors on CBZ removal by BC-AFe_2O_4/PAA

Different factors influencing CBZ removal in this system were evaluated to optimize the degradation performance of CBZ in the BC-AFe_2O_4 system. As shown in Figs. 4 and S9, the CBZ removal efficiency increased from 3 % to 100 %, and the K_{obs} of CBZ increased from 0.002 min^{-1} to 0.36 min^{-1} with increasing PAA concentration from 0 mM to 0.8 mM in the BC-$CoFe_2O_4$/PAA system. These results indicate that higher PAA concentrations generate more active species in these catalytic processes for the degradation of CBZ. However, the degradation efficiency of CBZ slightly decreased when the PAA concentration further increased to 1.2 mM and 1.6 mM, which can be attributed to excess PAA quenching the active species in the BC-$CoFe_2O_4$/PAA system. In addition, the H_2O_2 concentration increased with increasing PAA concentration since the commercial PAA solution contained both PAA and H_2O_2. It has also been proven (Eqs. (1)–(3)) that a relatively high concentration of H_2O_2 can scavenge active radicals, including $CH_3C(O)OO^{\bullet}$ and $CH_3C(O)O^{\bullet}$ [41]. Hence, the degradation rate of CBZ slightly decreases because of the low oxidizing capacity of $HO_2^{\bullet}$. Similar results were reported by Zhang et al. [42], who reported that the degradation efficiency of 2,4-dichlorophenol increased from 0.057 min^{-1} to 0.17 min^{-1} as the PAA concentration increased from 0.05 mM to 0.26 mM, while the degradation efficiency was slightly inhibited when the PAA concentration reached 1.04 mM in the Co@MXenes/PAA system. Moreover, the degradation efficiency of CBZ increased insignificantly as the PAA concentration increased from 0 mM to 1.6 mM in the BC-$CuFe_2O_4$/PAA and BC-$MnFe_2O_4$/PAA systems (Figs. S10a and S11a), which can be ascribed to the fact that neither BC-$CuFe_2O_4$ nor BC-$MnFe_2O_4$ can efficiently activate PAA for the degradation of organic pollutants under such conditions.

$$H_2O_2 + CH_3C(O)OO^{\bullet} \rightarrow HO_2^{\bullet} + CH_3C(O)OOH \quad (1)$$

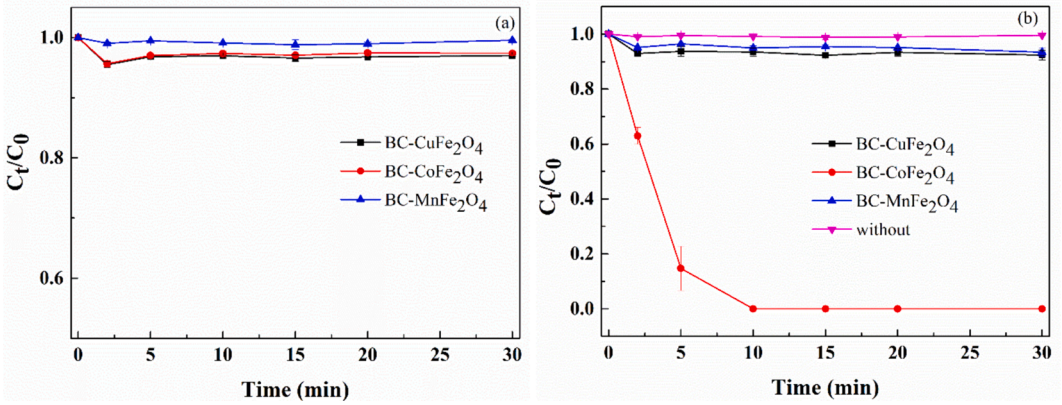

Fig. 3. Adsorption (a) and degradation (b) efficiencies of CBZ by different systems. Conditions: 0.3 g/L nanomaterials, 4 mg/L CBZ, 0.8 mM PAA.

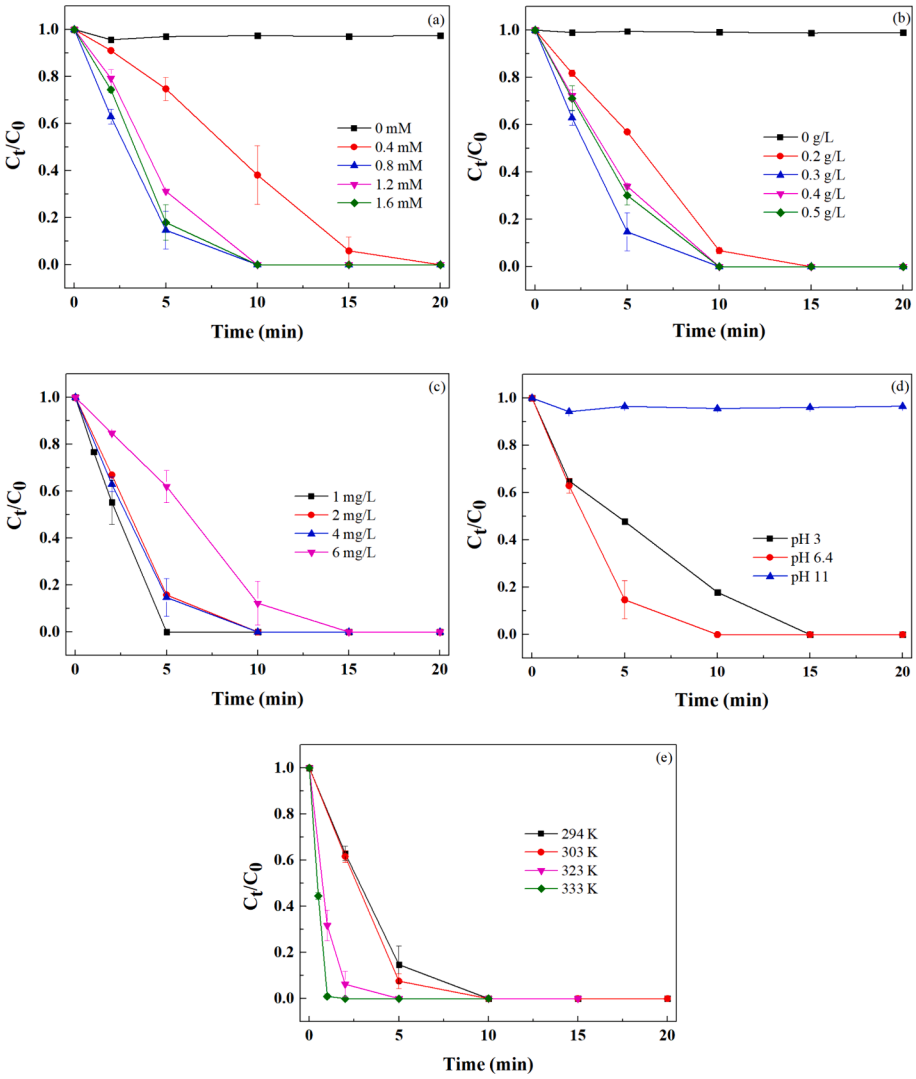

Fig. 4. Effects of the PAA concentration (a), BC-$CoFe_2O_4$ dose (b), CBZ concentration (c), initial pH (d), and solution temperature (e) on CBZ degradation in the BC-$CoFe_2O_4$/PAA system. Conditions: 0.8 mM PAA except (a), 0.3 g/L BC-$CoFe_2O_4$ except (b), 4 mg/L CBZ except (c), initial pH = 6.4 except (d), temperature 294 K except (e).

$$H_2O_2 + CH_3C(O)O^{\bullet} \rightarrow HO_2^{\bullet} + CH_3C(O)OH \quad (2)$$

$$O_2^{\bullet -} + CH_3C(O)OO^{\bullet} \rightarrow O_2 + CH_3C(O)OO^{-} \quad (3)$$

The effects of catalyst dosage on the degradation of CBZ in the BC-AFe_2O_4 system were also investigated. According to Figs. 4b and S9b, the degradation efficiency of CBZ increased obviously from 1 % to 100 % as the catalyst dose increased from 0 g/L to 0.3 g/L in the BC-$CoFe_2O_4$/PAA system, implying that the self-activation of PAA cannot efficiently degrade CBZ. An increase in the catalyst dose also provides more active sites for the activation of PAA; hence, more active species are expected under such conditions to accelerate CBZ degradation. However, the degradation efficiency of CBZ decreased when the catalyst concentration further increased to 0.4 g/L and 0.5 g/L, which could be related to the agglomeration of the nanomaterials due to magnetic gathering effects. Thus, the loss of surface active sites on the catalyst results in the low generation of active species and, consequently, low CBZ degradation efficiency in such a system [43]. Furthermore, increasing the catalyst concentration from 0.0 g/L to 0.5 g/L had no significant effect on the removal of CBZ using the BC-$CuFe_2O_4$ and BC-$MnFe_2O_4$ catalysts (Figs. S10b and S11b). This can further confirm the low efficiencies of these catalysts for the activation of PAA.

The effects of different CBZ concentrations on the BC-$CoFe_2O_4$/PAA system were also analyzed, as shown in Figs. 4c and S9c. The degradation rate of CBZ decreased from 0.39 to 0.18 min^{-1} as the CBZ concentration increased from 1 to 6 mg/L. This is due to the existence of relatively fewer oxidative species generated by the catalytic oxidation process for the degradation of more CBZ molecules present in the medium [44]. Similar trends were also observed in the present study for BC-$CuFe_2O_4$ and BC-$MnFe_2O_4$ at different concentrations of CBZ (Figs. S10c and S11c). However, in the latter cases, the degradation efficiency of CBZ was still poor even at a low CBZ concentration of 1 mg/L (14 % removal efficiency for both BC-$CuFe_2O_4$ and BC-$MnFe_2O_4$).

This study was further extended to investigate the effects of the solution pH on the degradation of CBZ in the BC-AFe_2O_4/PAA system. As illustrated in Figs. 4d and S9d, BC-$CoFe_2O_4$ displayed excellent degradation performance for CBZ (0.36 min^{-1}) at near-natural pH (initial pH), but the degradation efficiency decreased to 0.17 min^{-1} and 0.003 min^{-1} at pH values of 3 and 11, respectively. These observations can be ascribed to the surface charge of the catalyst and the dissociation of PAA at different pH values. The dissociation constant (K_a) of PAA was approximately 8.2 (Fig. S13), indicating that the dominant species of PAA are acid ($CH_3C(O)OOH$) and conjugate base ($CH_3CO_3^-$) at pH values of 3 and 11, respectively [16]. The acid species of PAA are too stable to

be easily activated in this system, resulting in a low generation of active species. In addition, the electrostatic repulsion effects between the catalyst (the potential of zero charge of BC-$CoFe_2O_4$ is approximately 5.5 (Fig. S12b)) and PAA are enhanced at pH 3, resulting in PAA being difficult to attach to the surface of BC-$CoFe_2O_4$. The concentration of free Co^{2+} also increased in the medium at pH 3, which accelerated the activation of PAA. Together, these abovementioned factors led to a decrease in the degradation efficiency of CBZ in the BC-$CoFe_2O_4$/PAA system at pH 3. Furthermore, the CBZ degradation efficiency significantly decreased at pH 11, which can be explained by the following factors. First, the interactions between BC-$CoFe_2O_4$ and PAA are inhibited due to the electrostatic repulsion effect between the negative surface charge of BC-$CoFe_2O_4$ and the conjugate base species of PAA. Second, the fast hydrolysis of PAA occurs via a nonradical process (Eqs. (4)–(6) under alkaline conditions, leading to rapid consumption of PAA [45]. Third, cobalt hydroxide is generated readily when the solution pH exceeds 8, and it is a dominant form when the solution pH is greater than 9.5. Hence, the amount of free Co^{2+} ions in the medium decreases, and the unreactive cobalt hydroxide complexes on the surface of the nanomaterials inhibit their catalytic activity. Accordingly, alkaline conditions, particularly strongly alkaline conditions, hinder the degradation of CBZ in the BC-$CoFe_2O_4$/PAA system. Furthermore, the effects of different solution pH values in the BC-$CuFe_2O_4$/PAA and BC-$MnFe_2O_4$/PAA systems on the degradation of CBZ are depicted in Figs. S10d, S11d, and S12a, c. According to the results, no significant changes in the efficiency of the abovementioned systems were observed by changing the pH of the medium.

$$CH_3C(O)OOH + CH_3C(O)OO^- \rightarrow CH_3C(O)OH + CH_3C(O)O^- + O_2 \quad (4)$$

$$CH_3C(O)OOH + H_2O \rightarrow CH_3C(O)OH + H_2O_2 \quad (5)$$

$$CH_3C(O)OO^- + H_2O_2 \rightarrow CH_3C(O)O^- + H_2O + O_2 \quad (6)$$

The effects of the reaction temperature on the degradation of CBZ in the BC-AFe_2O_4/PAA system were also explored. As depicted in Figs. 4e and S9e, the degradation rate constant of CBZ increased sharply from 0.36 min^{-1} to 1.62 min^{-1} when the operating temperature increased from 294 K to 333 K in the BC-$CoFe_2O_4$/PAA system. As illustrated in Fig. S9f, the thermally activated PAA process (without a catalyst) for the degradation of CBZ was less effective in the present study. Hence, the improved degradation efficiency can be attributed to the increased diffusion rate and mass transfer between the nanomaterials, PAA, and CBZ, thus accelerating the degradation efficiency of CBZ in this system [46]. In addition, the activation energy of CBZ degradation (0.8 mM PAA, 0.3 g/L BC-$CoFe_2O_4$, 4 mg/L CBZ, initial pH = 6.5) was 33.77 kJ/mol, which is similar to that in a previous report of 35.6 kJ/mol (an ultrasound/FeS/persulfate/CBZ system) [47] and 40.96 kJ/mol (a Co_3MnFeO_6/peroxymonosulfate/CBZ system) [48]. As depicted in Figs. S10e and S11e, a high temperature is not favorable for the degradation of CBZ in the BC-$CuFe_2O_4$/PAA system or BC-$MnFe_2O_4$/PAA system, revealing that BC-$CuFe_2O_4$ and $MnFe_2O_4$ cannot efficiently activate PAA for the degradation of CBZ under such conditions. In conclusion, operation parameters, including the PAA concentration, catalyst dosage, CBZ concentration, solution pH, and reaction temperature, play important roles in the degradation of CBZ in the BC-$CoFe_2O_4$/PAA system, but these parameters have a minor effect on the degradation of CBZ in the BC-$CuFe_2O_4$/PAA and BC-$MnFe_2O_4$/PAA systems.

3.4. Reaction mechanisms

In general, the activation process of PAA by BC-$CoFe_2O_4$ is relatively complicated since multiple active species, including singlet oxygen ($^1O_2$), $^{\bullet}OH$, and R-$O^{\bullet}$ (e.g., $CH_3C(O)OO^{\bullet}$, $CH_3C(O)O^{\bullet}$, $CH_3O_2^{\bullet}$, and $^{\bullet}CH_3$), with different reactivities are generated via chain reactions during the degradation process. Scavenging experiments were conducted to identify the primary active species responsible for the degradation of CBZ. It has been previously reported that methyl alcohol (MeOH) is a scavenger for $^{\bullet}OH$ and R-$O^{\bullet}$, while *tert*-butyl-alcohol (TBA) quenches only $^{\bullet}OH$ [49]. Furfuryl alcohol (FFA) is a widely used scavenger for $^1O_2$ with a rate constant of 1.2×10^8 M^{-1} S^{-1} [50]. As shown in Figs. S14–S16, the presence of MeOH and TBA had little effect on the PAA activation process, implying that the addition of MeOH and TBA is only responsible for quenching free species in the $CoFe_2O_4$/PAA system. In addition, although FFA slightly accelerated the decomposition of PAA, this effect was negligible compared with that of the BC-$CoFe_2O_4$-activated PAA process. Hence, these scavengers are highly reliable for quenching the active species in the $CoFe_2O_4$/PAA system.

Figs. 5 and S17 show that the addition of MeOH significantly inhibited the degradation efficiency of CBZ in the $CoFe_2O_4$/PAA system, while the presence of TBA slightly prevented the degradation of CBZ. These results indicate that $^{\bullet}OH$ plays an insignificant role in the degradation of CBZ, and R-$O^{\bullet}$ are the crucial radicals during CBZ degradation. In addition, the degradation efficiency of CBZ decreased sharply after the addition of FFA, suggesting that $^1O_2$ is the primary species responsible for the degradation of CBZ. However, previous reports confirmed that Co^{2+} is not responsible for the generation of $^1O_2$ [51]; hence, the majority of the $^1O_2$ was produced by self-decomposition reactions of PAA (Eq. (7)). In addition, both the BC-$CuFe_2O_4$/PAA and BC-$MnFe_2O_4$/PAA systems demonstrated a low CBZ degradation efficiency (Fig. 3), suggesting that the amount of $^1O_2$ generated from such self-decomposition reactions is not sufficient for the degradation of CBZ. Hence, the effect of $^1O_2$ on CBZ degradation can also be ignored in the BC-$CoFe_2O_4$/PAA system. Hence, R-$O^{\bullet}$ may be responsible for the degradation of CBZ in the BC-$CoFe_2O_4$/PAA system. The self-decomposition of $CH_3C(O)O^{\bullet}$ generates $^{\bullet}CH_3$ (Eq. (8), $k = 2.3 \times 10^5$ S^{-1}), which is highly unstable in the presence of oxygen and reacts with oxygen to form $CH_3O_2^{\bullet}$ (Eq. (9), $k = 4.1 \times 10^9$ M^{-1} S^{-1}) [52]. Additionally, $CH_3O_2^{\bullet}$ demonstrated relatively low reactivities for most organic pollutants (e.g., methylene blue, sulfamethoxazole, CBZ) with low reaction rate constants ($10^5 \sim 10^7$ M^{-1} S^{-1}) [53], suggesting that both $CH_3O_2^{\bullet}$ and $^{\bullet}CH_3$ are not responsible for the degradation of CBZ in the $CoFe_2O_4$/PAA system. In addition, $CH_3C(O)O^{\bullet}$ displays lower reaction constants ($10^5 \sim 10^7$ M^{-1} S^{-1}) for most organic pollutants (e.g., barbituric acid and uric acid) than $CH_3C(O)OO^{\bullet}$ ($10^7 \sim 10^9$ M^{-1} S^{-1}), implying that $CH_3C(O)OO^{\bullet}$ plays a more critical role in the degradation of CBZ in the $CoFe_2O_4$/PAA system. The degradation of CBZ by $CH_3C(O)O^{\bullet}$ is highly dependent on the β-cleavage reaction rate constant [40], which is comprehensively discussed in Text S8, and it also confirms that the effect of $CH_3C(O)O^{\bullet}$ on the degradation of CBZ can be ignored in the BC-$CoFe_2O_4$/PAA system. In conclusion, $CH_3C(O)OO^{\bullet}$ is the primary radical responsible for CBZ degradation in this system.

$$CH_3C(O)OOH + CH_3C(O)OO^- \rightarrow CH_3C(O)OH + CH_3C(O)O^- + {}^1O_2 \quad (7)$$

$$CH_3C(O)O^{\bullet} \rightarrow {}^{\bullet}CH_3 + CO_2 \quad (8)$$

$${}^{\bullet}CH_3 + O_2 \rightarrow CH_3O_2^{\bullet} \quad (9)$$

In situ ATR-FTIR analysis was conducted to further understand the interactions between BC-$CoFe_2O_4$ and PAA. As shown in Fig. S18, the intensities of the characteristic peaks at 1715 cm^{-1}, 1387 cm^{-1}, and 1274 cm^{-1} in the spectrum of the PAA solution increased with increasing PAA concentration, which can be assigned to the stretching vibration of the carbonyl group (C═O) [54], C–H in-plane bending vibration [55], and moderate C–H bending of PAA [56], respectively. The characteristic peaks of PAA exhibit an apparent shift, and the intensity of these peaks also decreased in the presence of BC-$CoFe_2O_4$, revealing that BC-$CoFe_2O_4$ activated PAA in the medium. The characteristic peak of –OH stretching vibrations at approximately 3500 cm^{-1} in the spectrum of the PAA solution became increasingly wider after the reaction with BC-$CoFe_2O_4$, indicating the formation of –OH groups on the surface of BC-$CoFe_2O_4$, and these groups were involved in the PAA activation

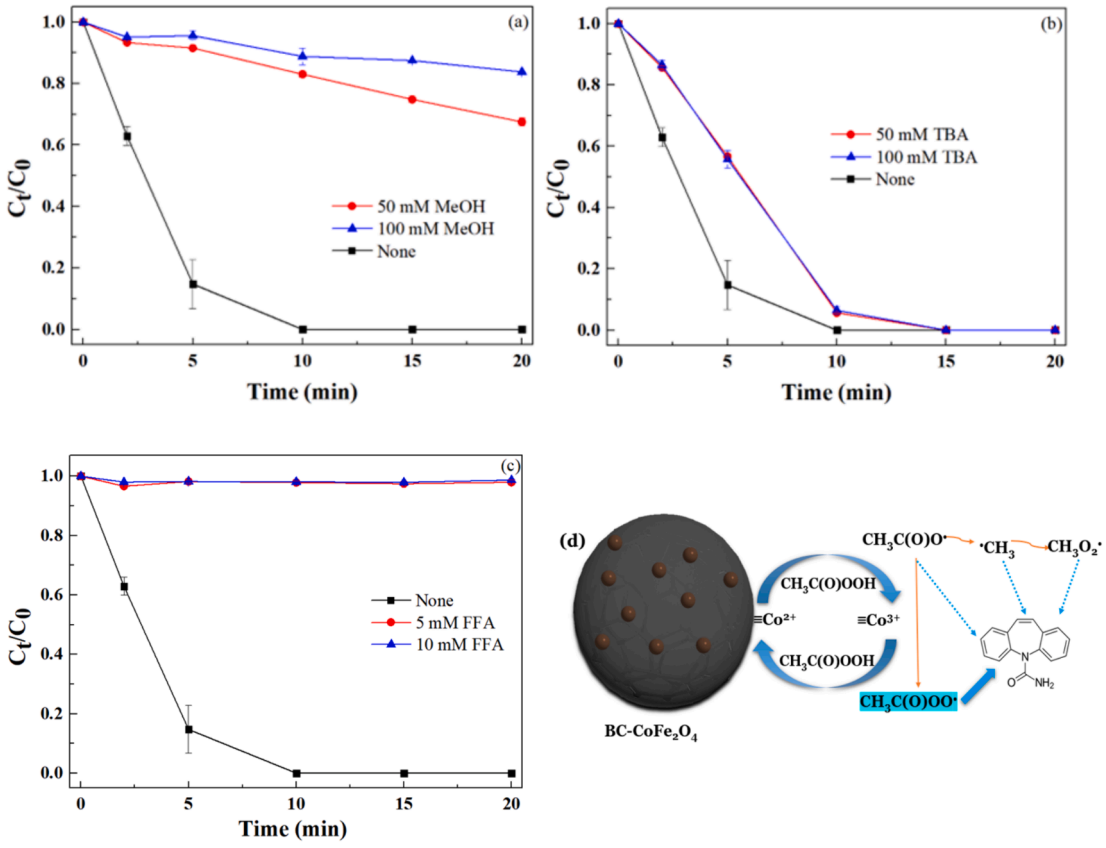

Fig. 5. Effects of different scavengers (a–c) on CBZ degradation in the BC-$CoFe_2O_4$/PAA system. Conditions: 4 mg/L CBZ, 0.8 Mm PAA, 0.3 g/L nanomaterials. The proposed mechanisms for CBZ degradation in the BC-$CoFe_2O_4$/PAA system.

process. Similar results were reported by Zhang et al. [40], who reported that $CH_3C(O)O^{\bullet}$ was generated from the split O–O bond of PAA and the remaining –OH groups on the CuO surface in the CuO/PAA system. Moreover, CV tests were carried out to further investigate the reaction mechanisms in the BC-$CoFe_2O_4$/PAA system. As shown in Fig. S19, a noticeable reduction peak was observed after the addition of PAA, indicating that redox was coupled with PAA activation in the BC-$CoFe_2O_4$/PAA system. Guo et al. [57] observed that the intensity of the oxidation peak increased in the presence of persulfate in the MnO_x/persulfate system, suggesting that Mn^{3+}/Mn^{4+} redox was involved in the activation process of persulfate in this system.

According to the above discussion, it can be concluded that $CH_3C(O)OO^{\bullet}$ is generated from the redox reaction between BC-$CoFe_2O_4$ and PAA, which is responsible for the degradation of CBZ in the BC-$CoFe_2O_4$/PAA system. Hence, a possible mechanism for the activation of PAA was proposed, as shown in Fig. 5d. In the preliminary stage, PAA can accept one electron from the surface of $\equiv Co^{2+}$ via Eq. (10), resulting in the formation of $CH_3C(O)O^{\bullet}$. Moreover, $\equiv Co^{3+}$ can also react with PAA to produce $CH_3C(O)OO^{\bullet}$ via Eq. (11), which is beneficial for the continuous conversion of $\equiv Co^{2+}/\equiv Co^{3+}$ on the surface of BC-$CoFe_2O_4$. Although $CH_3C(O)O^{\bullet}$ can react with PAA via Eq. (12), the rate constant ($(0.01–1) \times 10^7$ M^{-1} S^{-1})) is less than the reaction rate constant for self-decomposition of $CH_3C(O)O^{\bullet}$ (Eqs. (8) and (9)) [58], indicating that $CH_3C(O)O^{\bullet}$ is not involved in the PAA decomposition process. Therefore, most of the PAA is consumed through the reaction of $\equiv Co^{2+}$ and $\equiv Co^{3+}$. Notably, Fe^{3+} can also react with PAA for the degradation of CBZ (Fig. S7), but the contributions of Fe^{3+} are insignificant in the BC-$CoFe_2O_4$/PAA system due to the much lower reaction rate of Fe^{3+} with PAA compared with that of Co^{2+} (Fig. S7) and the lower concentration of iron ions under near-neutral pH conditions. Dong et al. [19] also reported that the contributions of Fe^{2+}/Fe^{3+} to the degradation of sulfamethoxazole in the BC (derived from lignin)-$CoFe_2O_4$/PAA system are very limited. Furthermore, the high surface area of BC provides more active sites for the activation of PAA in the CBZ degradation process, and the surface functional groups of BC accelerate the movement of electrons in the BC-$CoFe_2O_4$/PAA system, which improves the degradation efficiency of CBZ in this medium [59].

$$\equiv Co^{2+} + CH_3C(O)OOH \rightarrow \equiv Co^{3+} + CH_3C(O)O^{\bullet} + OH^- \quad (10)$$

$$\equiv Co^{3+} + CH_3C(O)OOH \rightarrow \equiv Co^{2+} + CH_3C(O)OO^{\bullet} + H^+ \quad (11)$$

$$CH_3C(O)OOH + CH_3C(O)O^{\bullet} \rightarrow CH_3C(O)OO^{\bullet} + CH_3C(O)OH \quad (12)$$

3.5. Effects of water matrices on CBZ removal by BC-$CoFe_2O_4$/PAA

CBZ-contaminated real wastewater normally contains natural organic matter (e.g., HA) and different ions (e.g., Cl^-, HCO_3^-, NO_3^-), which may compete with CBZ for the active sites of nanomaterials and active species in the medium during the degradation process. Hence, this work also considered the influence of natural organic matter and different ions on the degradation of CBZ in the BC-$CoFe_2O_4$/PAA system. HA, as a macromolecular organic pollutant, normally displays a complex structure and non-biodegradation characteristics [60]. The effects of HA on CBZ degradation in this system are depicted in Figs. 6a and S20. The CBZ degradation efficiency after 20 min decreased significantly from 100 % to 74 % when the HA concentration increased from 0 mg/L to 50 mg/L. This can be attributed to the fact that HA can occupy the active sites of BC-$CoFe_2O_4$ through complexation effects, resulting in insufficient active sites for the activation of PAA. In addition, previous studies confirmed that HA scavenges R-$O^{\bullet}$ radicals in the medium (10^4 L mg^{-1} s^{-1}) [61], leading to the active species being insufficiently present in the medium for the degradation of CBZ. In Fig. 6b, the CBZ degradation

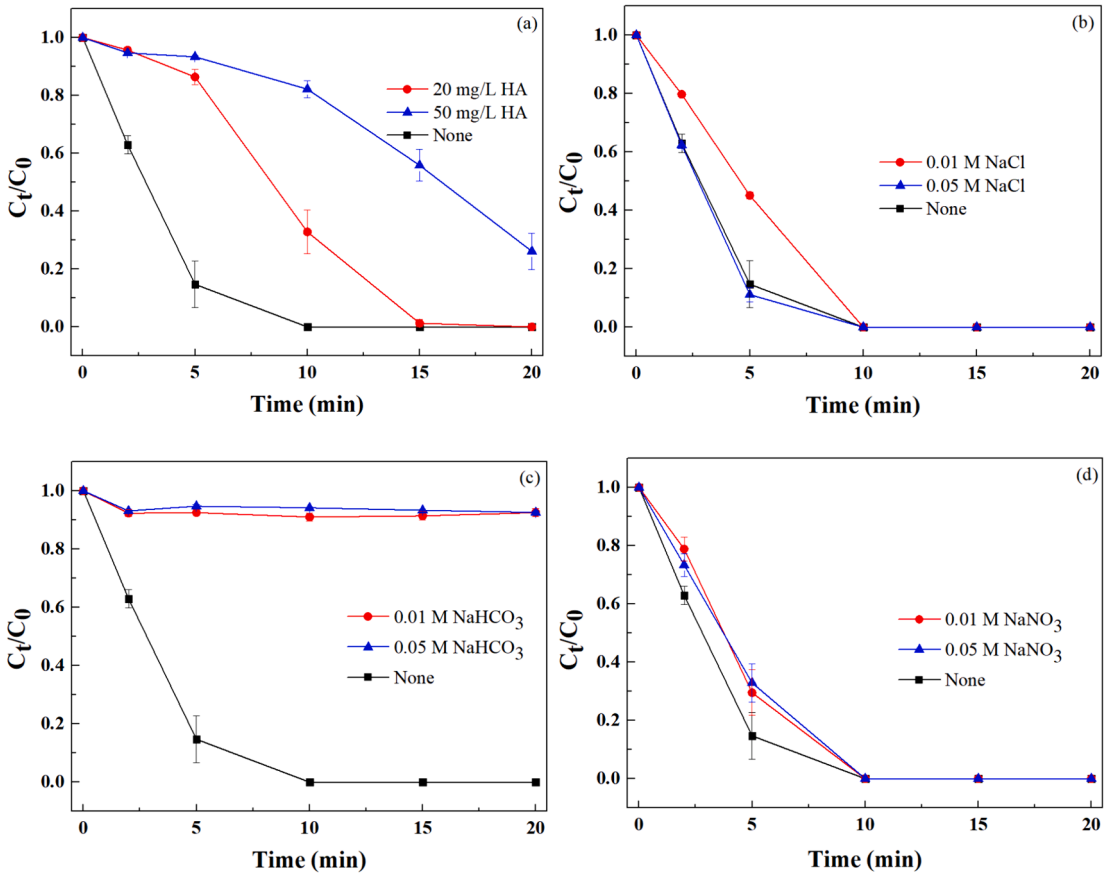

Fig. 6. Effects of HA (a), NaCl (b), $NaHCO_3$ (c), and $NaNO_3$ (d) on CBZ degradation in the BC-$CoFe_2O_4$/PAA system. Conditions: 4 mg/L CBZ, 0.8 mM PAA, 0.3 g/L nanomaterials.

efficiency is slightly suppressed at a relatively low Cl^- concentration in the BC-$CoFe_2O_4$/PAA system, which can be attributed to the competition of active sites and species between CBZ and Cl^-. Interestingly, CBZ degradation was hardly affected at a relatively high Cl^- concentration in this system, which can be related to the formation of chlorine-containing radicals ($Cl^{\bullet}$, $Cl_2^{\bullet-}$) via Eqs. (13) and (14), implying that these radicals also take part in the degradation process of CBZ in this medium. Similar results have been observed for the degradation of sulfamethoxazole in the zero-valent cobalt/PAA system [45]. In Fig. 6c, the presence of HCO_3^- significantly inhibited CBZ degradation in the $CoFe_2O_4$/PAA system, which can be ascribed to the scavenging effects of HCO_3^- on $^{\bullet}OH$ via Eq. (15). In addition, the formation of unreactive Co^{2+}–HCO_3^- complexes reduces the free Co^{2+} in the medium, resulting in a low generation of active species and a decreased degradation efficiency of CBZ. Deng et al. [62] also reported that the degradation efficiency of diclofenac was inhibited in the presence of HCO_3^- in a phosphate/PAA system. As shown in Fig. 6d, the presence of NO_3^- had a negligible effect on CBZ degradation in the $CoFe_2O_4$/PAA system, which can be attributed to the fact that NO_3^- hardly reacts with the active species (e.g., $CH_3C(O)OO^{\bullet}$) in the medium. In conclusion, the $CoFe_2O_4$/PAA system can be considered a potential promising candidate for the treatment of CBZ-containing real wastewater.

$$CH_3C(O)OO^{\bullet} + Cl^- + H^+ \rightarrow CH_3C(O)OOH + Cl^{\bullet} \quad (13)$$

$$Cl^{\bullet} + Cl^- \rightarrow Cl_2^{\bullet-} \quad (14)$$

$$^{\bullet}OH + HCO_3^- \rightarrow CO_3^{\bullet-} + H_2O \quad (15)$$

3.6. Degradation intermediate analysis and toxicity evaluation

The transformation products of CBZ in the BC-$CoFe_2O_4$/PAA system were determined by using UHPLC-DAD-QTOF-MS. Seven degradation products were identified, as summarized in Table S4. In addition, the time-dependent evolution of major products is presented in Fig. S21. The relative peak area (based on the initial CBZ peak area) of product P1 increased more obviously than that of the other degradation products, revealing that P1 may be the major intermediate during CBZ degradation. The proposed degradation pathways of CBZ are illustrated in Fig. 7. The olefinic double bond of CBZ, which has a high frontier electron density, is considered the primary reactive site and can be easily attacked by active species (e.g., $CH_3C(O)OO^{\bullet}$) [63]. Hence, the products P1 and P2 could be generated by $CH_3C(O)OO^{\bullet}$ attacking the olefinic double bond in the central heterocyclic ring of CBZ. Subsequently, the intermediate of P3 was produced from P2 through the cleavage and oxidation of the heterocyclic ring. The generation of products P4 and P5 is also related to the further oxidation of P2, and intermediate P6 could be generated through the cleavage of the aldehyde group of P5. Finally, these intermediates can be oxidized into small compounds (e.g., P7).

The toxicity of CBZ and CBZ degradation intermediates in the BC-$CoFe_2O_4$/PAA system was assessed by using different factors, including acute toxicity, bioconcentration factor, developmental toxicity, and mutagenicity. As shown in Fig. 8a, intermediates P1, P4, P6, and P7 display lower acute toxicity than CBZ, but some intermediates, including P2, P3, and P5, still have high toxicity. In addition, most degradation products, except for P5 and P6, presented a decreased bioconcentration factor (Fig. 8b), indicating that the bioconcentration of these intermediates was lower than that of CBZ. As shown in Fig. 8c and d, three intermediates demonstrated a remarkable decrease in developmental

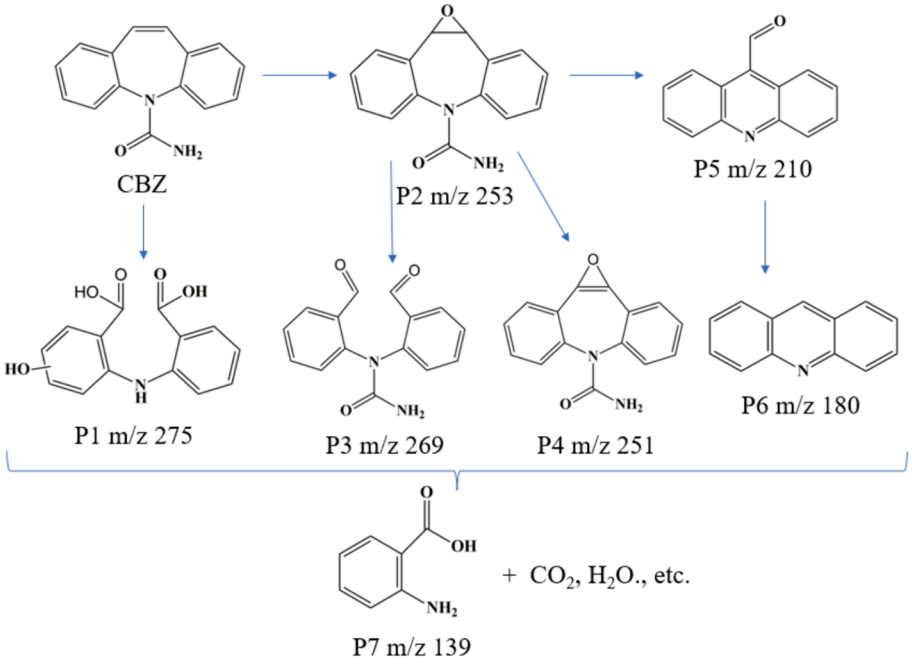

Fig. 7. Proposed CBZ degradation pathways in the BC-$CoFe_2O_4$/PAA system.

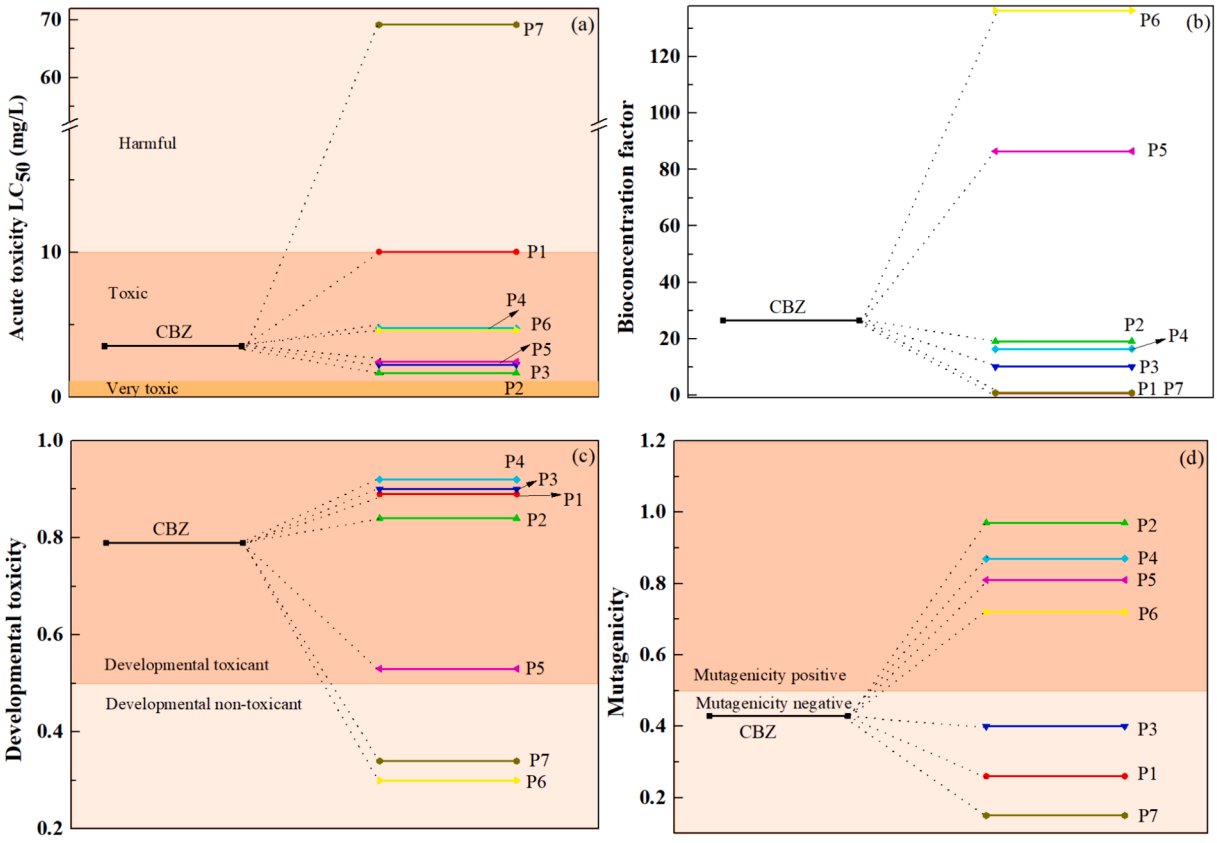

Fig. 8. Acute toxicity (a), bioconcentration factor (b), developmental toxicity (c), and mutagenicity (d) of CBZ and its degradation products.

toxicity compared with CBZ, and four degradation products were determined to be mutagenic. Notably, transformation products P1 and P2 were the major products of CBZ degradation (Fig. S21). Hence, the overall toxicity of CBZ degradation products is lower than that of CBZ, according to a comprehensive assessment of the toxicity results. However, more attention needs to be given to some degraded products that still have high toxicity to provide efficient complementary treatments. For instance, the concentration of intermediate P1 decreased after 15 min of CBZ degradation (Fig. S21), indicating that prolonging the reaction time can be considered an efficient method for solving this issue.

3.7. Applicability and stability of BC-$CoFe_2O_4$

The BC-$CoFe_2O_4$/PAA system was further evaluated for its ability to degrade various organic pollutants, including CBZ, sulfamethoxazole (SMX), 17-α-ethynylestradiol (EE2), ciprofloxacin (CIP), and diclofenac (DCF). The system demonstrated excellent degradation efficiencies for these pollutants (Fig. 9). Among all the treated pollutants, CBZ exhibited the best degradation performance, and CIP exhibited the worst degradation performance, suggesting that the active species may have selectivity for certain contaminants in this medium. It has also been reported that $CH_3C(O)OO^{\bullet}$ has high reactivity with electron-rich functional groups (e.g., primary amines or secondary amines), indicating that $CH_3C(O)OO^{\bullet}$ prefers to react with pollutants with electron-rich groups, which leads to rapid degradation of these organic pollutants. In addition, the relationship between the pollutant degradation kinetics and ionization potential was investigated. In general, the ionization potential of contaminants can be decreased by the addition of electron-rich groups (e.g., amine and hydroxyl). In contrast, this value can be increased with electron-withdrawing groups (e.g., nitryl and carboxyl) [64]. As shown in Table S5 and Fig. S22, a probable ionization potential threshold was identified at 7.2 eV, revealing that a pollutant with a high ionization potential (e.g., CIP > 7.2 eV) is difficult to degrade in this system. Such a selective degradation process based on the ionization potential values has also been reported for the Co-Fe bimetal catalyst/peroxymonosulfate system [65] and discharge plasma system [66].

The reusability and stability of the spent catalysts were also investigated, as illustrated in Figs. S23–S25. All BC-AFe_2O_4 materials exhibit outstanding magnetic properties and are hence easy to separate from treated water using a magnet. In addition, no significant decrease in CBZ degradation efficiency was observed after three recycling runs in the BC-$CoFe_2O_4$/PAA system. The FTIR spectra of fresh and used BC-$CoFe_2O_4$ demonstrated the same peaks (Fig. S25), indicating that BC-$CoFe_2O_4$ is a stable and recyclable activator for PAA. The effects of different water sources on CBZ degradation in the BC-$CoFe_2O_4$/PAA system are illustrated in Fig. S26a–c. The CBZ degradation efficiencies were significantly inhibited when tap water (0.06 min^{-1}) and real effluent (0.0047 min^{-1}) were used as the carrying media compared with ultrapure water (0.36 min^{-1}). This can be attributed to the fact that tap water and real effluents contain different ions, natural organic matter, and bacteria, which consume the active species in the medium, resulting in a low CBZ degradation efficiency in this system. At a high PAA concentration (2 mM), the CBZ removal efficiencies were improved in tap water (0.18 min^{-1}) and real effluents (0.042 min^{-1}). Hence, the BC-$CoFe_2O_4$/PAA system is a promising method for the treatment of real wastewater.

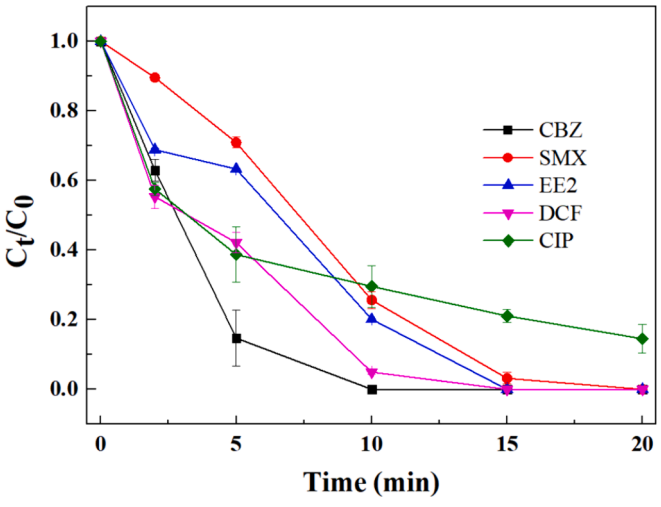

Fig. 9. Removal efficiencies of five typical organic pollutants in the BC-$CoFe_2O_4$ system. Conditions: 4 mg/L pollutants, 0.8 mM PAA, 0.3 g/L nanomaterials.

3.8. Removal of CBZ in dynamic systems

The degradation efficiency of CBZ was also evaluated in a continuous system, as shown in Fig. 10a. In this system, BC-$CoFe_2O_4$ was immobilized by using a permanent magnet, which can be considered a promising way to solve the recycling and separation problems of nanomaterials. The reaction time between the catalysts and PAA/pollutants was approximately 8 min based on the reactor volume and flow rate. The degradation efficiency of CBZ increases slowly with increasing cumulative volume and ultimately reaches a removal ratio of approximately 70 % (Fig. 10c). This can be attributed to the fact that the active species are insufficient for the degradation of CBZ due to the short contact time between BC-$CoFe_2O_4$ and PAA. As shown in Fig. 10d, the circular system (Fig. 10b) displays excellent degradation (97 %) of CBZ after 3 h, suggesting that BC-$CoFe_2O_4$ is stable and recyclable. In addition, the leaching of cobalt ions was 0.158 mg/L and 0.106 mg/L in the continuous system and circular system, respectively. The leaching of iron ions was less than 0.005 mg/L in both of the dynamic systems (Table S6). These values are much lower than the permissible discharge limit (1.0 mg/L) for industrial wastes according to the Chinese National Standard (GB 25467–2010) and Canadian Water Quality Guidelines [67,68]. Hence, it can be concluded that the BC-$CoFe_2O_4$/PAA system exhibits exceptional degradation of CBZ in dynamic systems, confirming that it provides a potential immobilization method for magnetic materials for water remediation in practical long-term reaction systems.

4. Conclusions

In the present study, novel magnetic biochar (BC)-ferrospinel AFe_2O_4 (A = Cu, Co, or Mn) nanocomposites were successfully synthesized and applied for the first time in PAA activation for the degradation of organic pollutants. Compared with BC-$MnFe_2O_4$ (7 %) and BC-$CuFe_2O_4$ (7 %), BC-$CoFe_2O_4$ demonstrated excellent carbamazepine degradation efficiency (100 %) in the presence of PAA. The continuous conversion of Co (II) to Co(III) promoted the generation of $CH_3C(O)OO^{\bullet}$ radicals, which are the primary active species for the degradation of CBZ in the BC-$CoFe_2O_4$/PAA system. In addition, the best conditions were obtained at 0.8 mM PAA, 0.3 g/L catalyst, 1 mg/L CBZ, near neutral pH, and 333 K in the BC-$CoFe_2O_4$/PAA system. The BC-$CoFe_2O_4$/PAA system also exhibited outstanding degradation efficiency for CBZ in the presence of humic acid (20 mg/L), NaCl (0.05 M), and $NaNO_3$ (0.01 M). It can degrade various recalcitrant organic contaminants (e.g., ciprofloxacin, sulfamethoxazole, 17-α-ethynylestradiol, and diclofenac sodium). Furthermore, the degradation products and possible degradation pathways of CBZ were proposed, and the overall toxicity of the transformation products was lower than that of CBZ based on the Toxicity Estimation Software Tool analysis. The recycling experiments also demonstrated that the BC-$CoFe_2O_4$/PAA system has high stability and can be used in dynamic systems and real wastewater treatment. This work provides an in-depth comparative study of BC-AFe_2O_4 for PAA activation and will facilitate the application and development of PAA-based AOPs in wastewater treatment.

CRediT authorship contribution statement

Yongtao Xue: Writing – original draft, Investigation, Formal analysis, Conceptualization. **Mohammadreza Kamali:** Writing – review & editing, Supervision, Methodology, Investigation. **Babak Kakavandi:** Writing – review & editing, Investigation, Conceptualization. **Maria Elisabete V. Costa:** Investigation, Formal analysis. **Ian P. Thompson:** Writing – review & editing, Methodology, Conceptualization. **Wei Huang:** Writing – review & editing, Methodology, Conceptualization. **Lise Appels:** Writing – review & editing, Methodology, Conceptualization. **Raf Dewil:** Writing – review & editing, Supervision, Methodology,

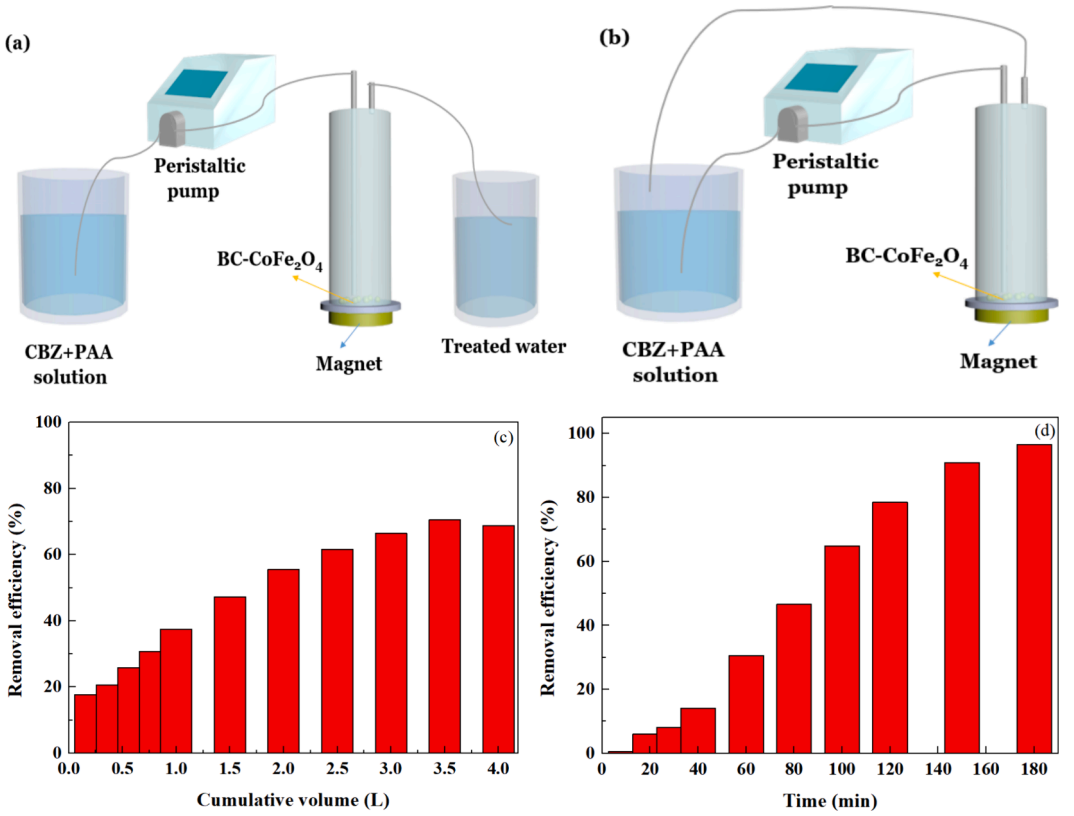

Fig. 10. Schematic illustration of the continuous system (a) and circular system (b), the removal efficiency of CBZ in the continuous system (c), and the circular system (d). Conditions: 0.1 g BC-$CoFe_2O_4$, 0.8 mM PAA, 1 mg/L CBZ, flow speed of 25 mL/min, total CBZ volume of 4 L, and reactor volume of 200 mL.

Conceptualization.

Declaration of competing interest

The authors declare that they have no known competing financial interests or personal relationships that could have appeared to influence the work reported in this paper.

Data availability

Data will be made available on request.

Acknowledgements

This work was supported by the China Scholarship Council (CSC) [grant number 202009505003].

Appendix A. Supplementary data

Supplementary data to this article can be found online at https://doi.org/10.1016/j.cej.2024.151932.

References

[1] Y. Xue, M. Kamali, A. Liyakat, M. Bruggeman, Z. Muhammad, B. Rossi, M.E. V. Costa, L. Appels, R. Dewil, A walnut shell biochar-nano zero-valent iron composite membrane for the degradation of carbamazepine via persulfate activation, Sci. Total Environ. 899 (2023) 165535, https://doi.org/10.1016/j.scitotenv.2023.165535.

[2] G.Z. Kyzas, N. Mengelizadeh, M.k. Saloot, S. Mohebi, D. Balarak, Sonochemical degradation of ciprofloxacin by hydrogen peroxide and persulfate activated by ultrasound and ferrous ions, Colloids Surf. A 642 (2022) 128627, https://doi.org/10.1016/j.colsurfa.2022.128627.

[3] X. Ao, J. Eloranta, C.-H. Huang, D. Santoro, W. Sun, Z. Lu, C. Li, Peracetic acid-based advanced oxidation processes for decontamination and disinfection of water: a review, Water Res. 188 (2021) 116479, https://doi.org/10.1016/j.watres.2020.116479.

[4] S. Correa-Sanchez, G.A. Peñuela, Peracetic acid-based advanced oxidation processes for the degradation of emerging pollutants: a critical review, J. Water Process Eng. 49 (2022) 102986, https://doi.org/10.1016/j.jwpe.2022.102986.

[5] J. Hollman, J.A. Dominic, G. Achari, Degradation of pharmaceutical mixtures in aqueous solutions using UV/peracetic acid process: kinetics, degradation pathways and comparison with UV/H_2O_2, Chemosphere 248 (2020) 125911, https://doi.org/10.1016/j.chemosphere.2020.125911.

[6] B. Zhang, W. Li, H. Zhang, B. Li, J. Ma, X. He, Activation of peracetic acid by trace ferrous ion and vacuum ultraviolet for the ultrafast degradation of PPCPs, ACS ES&T Water (2022), https://doi.org/10.1021/acsestwater.2c00366.

[7] Z. Wang, Y. Fu, Y. Peng, S. Wang, Y. Liu, HCO3–/CO32– enhanced degradation of diclofenac by Cu(II)-activated peracetic acid: Efficiency and mechanism, Sep. Purif. Technol. 277 (2021) 119434, https://doi.org/10.1016/j.seppur.2021.119434.

[8] J. Kim, T. Zhang, W. Liu, P. Du, J.T. Dobson, C.-H. Huang, Advanced oxidation process with peracetic acid and Fe(II) for contaminant degradation, Environ. Sci. Tech. 53 (2019) 13312–13322, https://doi.org/10.1021/acs.est.9b02991.

[9] Z. Zhang, Y. Duan, C. Dai, S. Li, Y. Chen, Y. Tu, K.H. Leong, L. Zhou, Oxidation of sulfamethazine by peracetic acid activated with biochar: reactive oxygen species contribution and toxicity change, Environ. Pollut. 313 (2022) 120170, https://doi.org/10.1016/j.envpol.2022.120170.

[10] J. Kim, C.-H. Huang, Reactivity of peracetic acid with organic compounds: a critical review, ACS ES&T Water 1 (2021) 15–33, https://doi.org/10.1021/acsestwater.0c00029.

[11] T. Yan, Q. Ping, A. Zhang, L. Wang, Y. Dou, Y. Li, Enhanced removal of oxytetracycline by UV-driven advanced oxidation with peracetic acid: Insight into the degradation intermediates and N-nitrosodimethylamine formation potential, Chemosphere 274 (2021) 129726, https://doi.org/10.1016/j.chemosphere.2021.129726.

[12] K. Yao, L. Fang, P. Liao, H. Chen, Ultrasound-activated peracetic acid to degrade tetracycline hydrochloride: efficiency and mechanism, Sep. Purif. Technol. 306 (2023) 122635, https://doi.org/10.1016/j.seppur.2022.122635.

[13] G. Zhou, Y. Fu, R. Zhou, L. Zhang, L. Zhang, J. Deng, Y. Liu, Efficient degradation of organic contaminants by magnetic cobalt ferrite combined with peracetic acid, Process Saf. Environ. Prot. 160 (2022) 376–384, https://doi.org/10.1016/j.psep.2022.02.031.

[14] D. Yuan, K. Yang, S. Pan, Y. Xiang, S. Tang, L. Huang, M. Sun, X. Zhang, T. Jiao, Q. Zhang, B. Li, Peracetic acid enhanced electrochemical advanced oxidation for organic pollutant elimination, Sep. Purif. Technol. 276 (2021) 119317, https://doi.org/10.1016/j.seppur.2021.119317.

[15] C. Yu, L. Zheng, Y. Hong, J. Chen, F. Gao, Y. Zhang, X. Zhou, L. Yang, Activation of peracetic acid with $CuFe_2O_4$ for rhodamine B degradation: activation by Cu and the

contribution of acetylperoxyl radicals, Molecules 27 (2022), https://doi.org/10.3390/molecules27196385.
[16] J. Wang, B. Xiong, L. Miao, S. Wang, P. Xie, Z. Wang, J. Ma, Applying a novel advanced oxidation process of activated peracetic acid by $CoFe_2O_4$ to efficiently degrade sulfamethoxazole, Appl. Catal. B 280 (2021) 119422, https://doi.org/10.1016/j.apcatb.2020.119422.
[17] R. Roto, Y. Yusran, A. Kuncaka, Magnetic adsorbent of Fe_3O_4@SiO_2 core-shell nanoparticles modified with thiol group for chloroauric ion adsorption, Appl. Surf. Sci. 377 (2016) 30–36, https://doi.org/10.1016/j.apsusc.2016.03.099.
[18] Y. Xue, M. Kamali, S.M. Al-Salem, B. Rossi, L. Appels, R. Dewil, Naturally derived materials to enhance the membrane properties in (waste)water treatment applications – mechanisms, scale-up challenges and economic considerations, J. Water Process Eng. 57 (2024) 104647, https://doi.org/10.1016/j.jwpe.2023.104647.
[19] J. Dong, W. Xu, S. Liu, Y. Gong, T. Yang, L. Du, Q. Chen, X. Tan, Y. Liu, Lignin-derived biochar to support $CoFe_2O_4$: effective activation of peracetic acid for sulfamethoxazole degradation, Chem. Eng. J. 430 (2022) 132868, https://doi.org/10.1016/j.cej.2021.132868.
[20] D. Gupta, V. Rishi, T.K. Gupta, Synthesis of MFe2O4 (M: Cu, Mn Co, Ni) magnetic nanoparticles and their efficient catalytic role in nitrophenol reduction, Mater. Res. Innov. 25 (2021) 393–398, https://doi.org/10.1080/14328917.2020.1831145.
[21] Y. Ren, L. Lin, J. Ma, J. Yang, J. Feng, Z. Fan, Sulfate radicals induced from peroxymonosulfate by magnetic ferrospinel MFe2O4 (M=Co, Cu, Mn, and Zn) as heterogeneous catalysts in the water, Appl. Catal. B Environ. 165 (2015) 572–578, https://doi.org/10.1016/j.apcatb.2014.10.051.
[22] J. Li, J. Yan, G. Yao, Y. Zhang, X. Li, B. Lai, Improving the degradation of atrazine in the three-dimensional (3D) electrochemical process using CuFe2O4 as both particle electrode and catalyst for persulfate activation, Chem. Eng. J. 361 (2019) 1317–1332, https://doi.org/10.1016/j.cej.2018.12.144.
[23] R. Monsef, M. Ghiyasiyan-Arani, M. Salavati-Niasari, Design of magnetically recyclable ternary Fe_2O_3/$EuVO_4$/g-C_3N_4 nanocomposites for photocatalytic and electrochemical hydrogen storage, ACS Appl. Energy Mater. 4 (2021) 680–695, https://doi.org/10.1021/acsaem.0c02557.
[24] Y. Xue, M. Kamali, X. Yu, L. Appels, R. Dewil, Novel CuO/Cu2(V2O7)/V2O5 composite membrane as an efficient catalyst for the activation of persulfate toward ciprofloxacin degradation, Chem. Eng. J. (2022) 140201, https://doi.org/10.1016/j.cej.2022.140201.
[25] I. Nedkov, R.E. Vandenberghe, T.s. Marinova, P.h. Thailhades, T. Merodiiska, I. Avramova, Magnetic structure and collective Jahn-Teller distortions in nanostructured particles of CuFe2O4, Appl. Surf. Sci. 253 (2006) 2589–2596, https://doi.org/10.1016/j.apsusc.2006.05.049.
[26] M.V. López-Ramón, M.A. Álvarez, C. Moreno-Castilla, M.A. Fontecha-Cámara, Á. Yebra-Rodríguez, E. Bailón-García, Effect of calcination temperature of a copper ferrite synthesized by a sol-gel method on its structural characteristics and performance as Fenton catalyst to remove gallic acid from water, J. Colloid Interface Sci. 511 (2018) 193–202, https://doi.org/10.1016/j.jcis.2017.09.117.
[27] T. Huang, Z. Qiu, Z. Hu, X. Lu, Novel method of preparing hierarchical porous $CoFe_2O_4$ by the citric acid-assisted sol-gel auto-combustion for supercapacitors, J. Energy Storage 35 (2021) 102286, https://doi.org/10.1016/j.est.2021.102286.
[28] L. Liu, Z. Jiang, L. Fang, H. Xu, H. Zhang, X. Gu, Y. Wang, Probing the crystal plane effect of Co_3O_4 for enhanced electrocatalytic performance toward efficient overall water splitting, ACS Appl. Mater. Interfaces 9 (2017) 27736–27744, https://doi.org/10.1021/acsami.7b07793.
[29] J. Venturini, T.B. Wermuth, M.C. Machado, S. Arcaro, A.K. Alves, A. da Cas Viegas, C.P. Bergmann, The influence of solvent composition in the sol-gel synthesis of cobalt ferrite (CoFe2O4): a route to tuning its magnetic and mechanical properties, J. Eur. Ceram. Soc. 39 (2019) 3442–3449, https://doi.org/10.1016/j.jeurceramsoc.2019.01.030.
[30] M. Shi, R. Zuo, Y. Xu, Y. Jiang, G. Yu, H. Su, J. Zhong, Preparation and characterization of $CoFe_2O_4$ powders and films via the sol–gel method, J. Alloy. Compd. 512 (2012) 165–170, https://doi.org/10.1016/j.jallcom.2011.09.057.
[31] E.H.M. Sakho, S. Thomas, N. Kalarikkal, O.S. Oluwafemi, Dielectric and dye adsorption properties of luminescent-superparamagnetic MFe2O4 (M = Mn, Mg)/reduced graphene oxide composites, Ceram. Int. 44 (2018) 3904–3914, https://doi.org/10.1016/j.ceramint.2017.11.181.
[32] S.V. Bhandare, R. Kumar, A.V. Anupama, H.K. Choudhary, V.M. Jali, B. Sahoo, Annealing temperature dependent structural and magnetic properties of $MnFe_2O_4$ nanoparticles grown by sol-gel auto-combustion method, J. Magn. Magn. Mater. 433 (2017) 29–34, https://doi.org/10.1016/j.jmmm.2017.02.040.
[33] J. Li, H. Yuan, G. Li, Y. Liu, J. Leng, Cation distribution dependence of magnetic properties of sol–gel prepared $MnFe_2O_4$ spinel ferrite nanoparticles, J. Magn. Magn. Mater. 322 (2010) 3396–3400, https://doi.org/10.1016/j.jmmm.2010.06.035.
[34] D. Simonova, I. Karamancheva, Application of Fourier transform infrared spectroscopy for tumor diagnosis, Biotechnol. Biotechnol. Equip. 27 (2013) 4200–4207.
[35] P.P. Bera, S.A. Sandford, T.J. Lee, M. Nuevo, The calculated infrared spectra of functionalized hexamethylenetetramine (HMT) molecules, Astrophys. J. 884 (2019) 64, https://doi.org/10.3847/1538-4357/ab3c4f.
[36] K. Shetty, L. Renuka, H.P. Nagaswarupa, H. Nagabhushana, K.S. Anantharaju, D. Rangappa, S.C. Prashantha, K. Ashwini, A comparative study on $CuFe_2O_4$, $ZnFe_2O_4$ and $NiFe_2O_4$: morphology, impedance and photocatalytic studies, Mater. Today Proc. 4 (2017) 11806–11815, https://doi.org/10.1016/j.matpr.2017.09.098.
[37] Y. Xue, Y. Guo, X. Zhang, M. Kamali, T.M. Aminabhavi, L. Appels, R. Dewil, Efficient adsorptive removal of ciprofloxacin and carbamazepine using modified pinewood biochar – a kinetic, mechanistic study, Chem. Eng. J. 450 (2022) 137896, https://doi.org/10.1016/j.cej.2022.137896.
[38] M. Moothedan, K.B. Sherly, Surface properties of nano mesoporous lanthanum oxide synthesized by sol-gel method, Mater. Today:. Proc. 66 (2022) 2338–2341, https://doi.org/10.1016/j.matpr.2022.06.328.
[39] Z. Li, S. Ning, F. Hu, H. Zhu, L. Zeng, L. Chen, X. Wang, T. Fujita, Y. Wei, Preparation of VCo-MOF@MXene composite catalyst and study on its removal of ciprofloxacin by catalytically activating peroxymonosulfate: construction of ternary system and superoxide radical pathway, J. Colloid Interface Sci. 629 (2023) 97–110, https://doi.org/10.1016/j.jcis.2022.08.193.
[40] L. Zhang, J. Chen, Y. Zhang, Y. Xu, T. Zheng, X. Zhou, Highly efficient activation of peracetic acid by nano-CuO for carbamazepine degradation in wastewater: The significant role of H_2O_2 and evidence of acetylperoxy radical contribution, Water Res. 216 (2022) 118322, https://doi.org/10.1016/j.watres.2022.118322.
[41] Z. Wang, J. Wang, B. Xiong, F. Bai, S. Wang, Y. Wan, L. Zhang, P. Xie, M. R. Wiesner, Application of cobalt/peracetic acid to degrade sulfamethoxazole at neutral condition: efficiency and mechanisms, Environ. Sci. Technol. 54 (2020) 464–475, https://doi.org/10.1021/acs.est.9b04528.
[42] L. Zhang, J. Chen, Y. Zhang, Z. Yu, R. Ji, X. Zhou, Activation of peracetic acid with cobalt anchored on 2D sandwich-like MXenes (Co@MXenes) for organic contaminant degradation: high efficiency and contribution of acetylperoxyl radicals, Appl. Catal. B Environ. 297 (2021) 120475, https://doi.org/10.1016/j.apcatb.2021.120475.
[43] L. Niu, G. Zhang, G. Xian, Z. Ren, T. Wei, Q. Li, Y. Zhang, Z. Zou, Tetracycline degradation by persulfate activated with magnetic γ-Fe_2O_3/CeO_2 catalyst: performance, activation mechanism and degradation pathway, Sep. Purif. Technol. 259 (2021) 118156, https://doi.org/10.1016/j.seppur.2020.118156.
[44] M.-M. Chen, H.-Y. Niu, C.-G. Niu, H. Guo, S. Liang, Y.-Y. Yang, Metal-organic framework-derived CuCo/carbon as an efficient magnetic heterogeneous catalyst for persulfate activation and ciprofloxacin degradation, J. Hazard. Mater. 424 (2022) 127196, https://doi.org/10.1016/j.jhazmat.2021.127196.
[45] G. Zhou, R. Zhou, Y. Liu, L. Zhang, L. Zhang, Y. Fu, Efficient degradation of sulfamethoxazole using peracetic acid activated by zero-valent cobalt, J. Environ. Chem. Eng. 10 (2022) 107783, https://doi.org/10.1016/j.jece.2022.107783.
[46] P. Yang, S. Li, L. Xiaofu, A. Xiaojing, D. Liu, W. Huang, Singlet oxygen-dominated activation of peroxymonosulfate by CuO/MXene nanocomposites for efficient decontamination of carbamazepine under high salinity conditions: performance and singlet oxygen evolution mechanism, Sep. Purif. Technol. 285 (2022) 120288, https://doi.org/10.1016/j.seppur.2021.120288.
[47] W. Xiang, H. Chen, Z. Zhong, C. Zhang, X. Lu, M. Huang, T. Zhou, P. Yu, B. Zhang, Efficient degradation of carbamazepine in a neutral sonochemical FeS/persulfate system based on the enhanced heterogeneous-homogeneous sulfur-iron cycle, Sep. Purif. Technol. 282 (2022) 120041, https://doi.org/10.1016/j.seppur.2021.120041.
[48] L. Zhang, X. Zhao, C. Niu, N. Tang, H. Guo, X. Wen, C. Liang, G. Zeng, Enhanced activation of peroxymonosulfate by magnetic Co_3MnFeO_6 nanoparticles for removal of carbamazepine: efficiency, synergetic mechanism and stability, Chem. Eng. J. 362 (2019) 851–864, https://doi.org/10.1016/j.cej.2019.01.078.
[49] L. Zhang, Y. Fu, Z. Wang, G. Zhou, R. Zhou, Y. Liu, Removal of diclofenac in water using peracetic acid activated by zero valent copper, Sep. Purif. Technol. 276 (2021) 119319, https://doi.org/10.1016/j.seppur.2021.119319.
[50] M.-H. Li, L.-X. Zhao, M. Xie, N. Li, X.-L. Wang, R.-S. Zhao, J.-M. Lin, Singlet oxygen-oriented degradation of sulfamethoxazole by Li–Al LDH activated peroxymonosulfate, Sep. Purif. Technol. 290 (2022) 120898, https://doi.org/10.1016/j.seppur.2022.120898.
[51] B. Liu, W. Guo, W. Jia, H. Wang, S. Zheng, Q. Si, Q. Zhao, H. Luo, J. Jiang, N. Ren, Insights into the oxidation of organic contaminants by Co(II) activated peracetic acid: the overlooked role of high-valent cobalt-oxo species, Water Res. 201 (2021) 117313, https://doi.org/10.1016/j.watres.2021.117313.
[52] R. Li, K. Manoli, J. Kim, M. Feng, C.-H. Huang, V.K. Sharma, Peracetic acid–ruthenium(III) oxidation process for the degradation of micropollutants in water, Environ. Sci. Tech. 55 (2021) 9150–9160, https://doi.org/10.1021/acs.est.0c06676.
[53] J. Kim, J. Wang, D.C. Ashley, V.K. Sharma, C.-H. Huang, Enhanced Degradation of micropollutants in a peracetic acid–Fe(III) system with picolinic acid, Environ. Sci. Tech. 56 (2022) 4437–4446, https://doi.org/10.1021/acs.est.1c08311.
[54] K.I. Martínez, R. González, J.J. Soto, I. Rosales, Characterization by FTIR spectroscopy of degradation of polyethylene films exposed to CO_2 laser radiation and domestic composting, J. Phys. Conf. Ser. 1723 (2021) 12038, https://doi.org/10.1088/1742-6596/1723/1/012038.
[55] E. Raju, P. Jayaprakash, G. Vinitha, N.S. Devi, S. Kumaresan, Growth and characterization of 2-aminopyridinium malonate single crystal for photonic device applications, J. Mater. Sci.: Mater. Electron. 32 (2021) 21155–21163, https://doi.org/10.1007/s10854-021-06614-x.
[56] S. Kainat, S.R. Gilani, F. Asad, M.Z. Khalid, W. Khalid, M.M.A.N. Ranjha, S. P. Bangar, J.M. Lorenzo, Determination and comparison of phytochemicals, phenolics, and flavonoids in solanum lycopersicum using FTIR spectroscopy, Food Anal. Methods (2022), https://doi.org/10.1007/s12161-022-02344-w.
[57] P.-C. Guo, H.-B. Qiu, C.-W. Yang, X. Zhang, X.-Y. Shao, Y.-L. Lai, G.-P. Sheng, Highly efficient removal and detoxification of phenolic compounds using persulfate activated by MnO_x@OMC: synergistic mechanism and kinetic analysis, J. Hazard. Mater. 402 (2021) 123846, https://doi.org/10.1016/j.jhazmat.2020.123846.
[58] P. Zhang, X. Zhang, X. Zhao, G. Jing, Z. Zhou, Activation of peracetic acid with zero-valent iron for tetracycline abatement: the role of Fe(II) complexation with

tetracycline, J. Hazard. Mater. 424 (2022) 127653, https://doi.org/10.1016/j.jhazmat.2021.127653.
[59] L. Wu, Z. Li, P. Cheng, Y. She, W. Wang, Y. Tian, J. Ma, Z. Sun, Efficient activation of peracetic acid by mixed sludge derived biochar: critical role of persistent free radicals, Water Res. 223 (2022) 119013, https://doi.org/10.1016/j.watres.2022.119013.
[60] W. Zhang, Y. He, C. Li, X. Hu, S. Yang, X. You, W. Liang, Persulfate activation using Co/AC particle electrodes and synergistic effects on humic acid degradation, Appl. Catal. B Environ. 285 (2021) 119848, https://doi.org/10.1016/j.apcatb.2020.119848.
[61] S. Chen, M. Cai, Y. Liu, L. Zhang, L. Feng, Effects of water matrices on the degradation of naproxen by reactive radicals in the UV/peracetic acid process, Water Res. 150 (2019) 153–161, https://doi.org/10.1016/j.watres.2018.11.044.
[62] J. Deng, H. Wang, Y. Fu, Y. Liu, Phosphate-induced activation of peracetic acid for diclofenac degradation: kinetics, influence factors and mechanism, Chemosphere 287 (2022) 132396, https://doi.org/10.1016/j.chemosphere.2021.132396.
[63] J. Cai, J. Xie, L. Xing, L. Zhou, Q. Zhang, M. Zhou, Enhanced mechanism of carbamazepine degradation by electrochemical activation of persulfate in flow-through system, Sep. Purif. Technol. 301 (2022) 122021, https://doi.org/10.1016/j.seppur.2022.122021.
[64] Y. Chai, H. Dai, P. Zhan, Z. Liu, Z. Huang, C. Tan, F. Hu, X. Xu, X. Peng, Selective degradation of organic micropollutants by activation of peroxymonosulfate by Se@NC: role of Se doping and nonradical pathway mechanism, J. Hazard. Mater. (2023) 131202, https://doi.org/10.1016/j.jhazmat.2023.131202.
[65] Q.-T. Sun, B.-D. Xu, J. Yang, T.-T. Qian, H. Jiang, Layered oxides supported Co-Fe bimetal catalyst for carbamazepine degradation via the catalytic activation of peroxymonosulfate, Chem. Eng. J. 400 (2020) 125899, https://doi.org/10.1016/j.cej.2020.125899.
[66] H. Li, T. Li, S. He, J. Zhou, T. Wang, L. Zhu, Efficient degradation of antibiotics by non-thermal discharge plasma: highlight the impacts of molecular structures and degradation pathways, Chem. Eng. J. 395 (2020) 125091, https://doi.org/10.1016/j.cej.2020.125091.
[67] D. Gao, Y. Lu, Y. Chen, M. Bao, N. Xu, Novel CoFe2Px derived from $CoFe_2O_4$ for efficient peroxymonosulfate activation: switching the reaction route and suppressing metal leaching, Appl. Catal. B Environ. 309 (2022) 121234, https://doi.org/10.1016/j.apcatb.2022.121234.
[68] K.G.N. Quiton, Y.-H. Huang, M.-C. Lu, Recovery of cobalt and copper from single- and co-contaminated simulated electroplating wastewater via carbonate and hydroxide precipitation, Sustain. Environ. Res. 32 (2022) 31, https://doi.org/10.1186/s42834-022-00140-z.